Advanced Steel Construction – Vol. 21 No. 6 (2025) 488–499
DOI:10.18057/IJASC.2025.21.6.2

EXPERIMENTAL STUDY ON FATIGUE CRACK GROWTH RATE OF HIGH-STRENGTH STRUCTURAL STEELS

Zhao Fang [1], Fan Yang [2], Ai-Qun Li [2, 3, *], Wen-Jie Jia [4], Hai-Yi Yang [5] and Jing-Wen Yu [1]

[1] *School of Civil Engineering and Architecture, Nanjing Institute of Technology, Nanjing 211167, China*
[2] *School of Civil Engineering, Southeast University, Nanjing 210096, China*
[3] *Beijing Advanced Innovation Center for Future Urban Design, Beijing University of Civil Engineering and Architecture, Beijing 100044, China*
[4] *Jiangsu Hydraulic Research Institute, Yangzhou 225002, China*
[5] *School of Mechanics and Engineering Sciences, Shanghai University, Shanghai 200444, China*
** (Corresponding author: E-mail: liaiqun@bucea.edu.cn)*

ABSTRACT

The static tension test on smooth specimens and the fatigue crack growth rate test on CT specimens were conducted for two mild steels, Q235B and Q355B, and three high-strength steels, Q460C, Q550D and Q690D. The digital image correlation (DIC) technique was introduced and strain results around the crack tip were verified by finite element analysis. Material constants based on stress intensity factor (SIF) range and strain energy density factor (SEDF) range were obtained by fitting. A thorough survey of fatigue crack growth test results of high-strength steels in relevant literature was conducted and test results were compared. The scatter band upper bound of fatigue crack growth curves for each steel was obtained and compared with suggested curves in various design codes. The results show that the strains at the crack tip of specimens obtained by finite element analysis and DIC analysis are in good agreement with each other; The mean+2s curve in BS7910 and DNVGL-RP-210, along with the curves in WES2805 and IIW-2259-15, are all applicable to the design of the three high-strength steels, while the mean curve in BS7910 and DNVGL-RP-210 are not applicable and the curves suggested by ASME BPVC or JSME S NA1-2008 and FKM are too conservative; The crack growth rate slows down with the increase of the yield strength, demonstrating the trend of decrease in material constants m, n and |logC| while increase in |logA|, although the trend is not strictly followed; The scatter band upper bounds established based on either SIF or SEDF are applicable to fatigue crack growth analysis and design of the three high-strength steels.

ARTICLE HISTORY

Received: 30 November 2024
Revised: 22 February 2025
Accepted: 2 March 2025

KEYWORDS

Fatigue crack growth rate;
High-strength steel;
Digital image correlation;
Finite element analysis;
Strain energy density factor

1. Introduction

In recent years, high-strength steel has gained extensive attention, since it has been applied in various high-rise and long-span engineering structures including buildings, bridges, etc. However, high-strength steel is susceptible to fatigue crack growth at initial defects under cyclic loading, leading to structural fatigue failure. Therefore, it is indispensable to study the fatigue crack growth rate performance of high-strength steel.

Researchers started to pay attention to fatigue crack growth rate tests using compacted tension (CT) specimens made of different high-strength steels and obtained their material constants in Paris law based on stress intensity factor (SIF) range. Barsom et al.[1] investigated the fatigue crack growth rate of four high-strength steels, HY-80, HY130, 10Ni-Cr-Mo-Co and 12Ni-5Cr-3Mo, by fatigue test; Jesus et al.[2] compared the fatigue behavior between the S355 mild steel and the S690 high strength steel by fatigue crack growth test. The fatigue crack growth rate performance of high-strength steels in China including GB Q460, Q550, Q690 and Q960 were also presented; Tong et al.[3] studied the fatigue behavior of Q460C, Q550D, Q690D and Q960D by fatigue crack growth test; Ma et al.[4] conducted static tension and fatigue crack growth tests of base metal and welded joints of Q550E and established their growth models; Shen et al.[5] investigated fatigue crack growth behaviors of EH690 HSS welded joints in zones of base metal, heat affected zone and weld metal by fatigue crack growth test with various stress ratios; Guo et al.[6] studied the fatigue crack growth performance of Q690D HSS by the test on CT specimens with two plate thicknesses at three stress ratios.

The above researches provide valuable data for high-strength steel fatigue resistance design. However, if attention is paid to test data collection in these researches, it is found that conventional displacement data collecting devices such as extensometers were normally adopted during fatigue crack growth tests while some new non-contact displacement measuring methods like digital image correlation (DIC) were additionally introduced. Panwitt et al.[7] endeavored to measured fatigue crack growth path by DIC; Li et al.[8] proposed a method to determine crack tip position and fracture process zone in concrete based on DIC technique. The use of DIC in fatigue crack growth rate tests of high-strength steels has rarely been reported yet, since DIC is a relatively new method but a promising one.

However, it is worth noting that material constants in above literatures were obtained by fitting only based on a mean curve with a survival probability of 50%, which is absolutely unsafe for fatigue resistance design due to neglection of uncertainties during tests. Inspired by this, researchers began to establish scatter band upper bounds for crack growth curves. Some researchers even compared these upper bounds or mean curves with suggested ones in design codes. Zong et al.[9][10] obtained the fatigue crack growth constants of Q345D and Q690D with CT specimens considering a survival probability of 95% along with a confidence level of 95% and compared them with suggested values in BS7910; Song et al.[11] established fatigue crack growth curves of Ni-Cr-Mo-V steel base metal and welded joints considering strength mismatch effect and compared the mean curves with suggested ones in BS7910; Chen et al.[12] conducted fatigue crack growth tests on Q420C steel under constant amplitude of cyclic loading and compared them with those in BS 7910. However, the comparison of these test results with suggested curves was mostly limited to the code of BS 7910, though fatigue resistance design will surely benefit from the comparison with more codes.

In addition to the use of SIF in fracture analysis, strain energy density factor (SEDF) S is also widely used, which was proposed by Sih[13]. A more detailed comparison between these two approaches will be made in Section 6 in this study. Due to the lack of material constant data, the application of SEDF in fatigue crack growth analysis is rather limited, especially for the analysis of structural steel. Few researches were reported so far. Badaliance[14] postulated the crack growth rate to be a function of the SEDF range and correlated crack growth data of several different materials including the high-strength steel of HP9-4-30 and 300M; Shen[15] conducted fatigue crack growth rate test on CT specimens made of GB Q235B and obtained the material constants related to SEDF. Therefore, more material constant data of high-strength steels are most significant for SEDF approach in crack growth analysis.

To address all the problems raised above, the fatigue crack growth rate performance of structural steels of Q235B, Q355B, Q460C, Q550D and Q690D were studied by static tension test on smooth specimens and fatigue crack growth rate test on CT specimens in this paper. The DIC technique was introduced into the test and strain results around the crack tip were verified by finite element (FE) analysis. Material constants in both Paris law based on SIF range and crack growth rate equations based on SEDF range were obtained by fitting of test results. A thorough survey of fatigue crack growth test results of high-strength steels in relevant literature was conducted and test results were compared. The scatter band upper bound of fatigue crack growth curves for each steel was established and they were compared with suggested curves in various design codes.

The novelty of this study lies in three major aspects: (1) Both the mean and the upper bound of fatigue crack growth curves for Q235B, Q355B, Q460C, Q550D and Q690D were respectively obtained and they were comprehensively compared with suggested curves in various design codes to provide reference to fatigue resistance design in steel components and structures; (2) DIC as a new

non-contact measuring method was introduced into fatigue crack growth tests of high-strength steel and it was presented elaborately; (3) Material constants and curves for fatigue crack growth equations based on SEDF range were proposed for high-strength steels to guide fatigue crack growth analysis based on SEDF.

2. Static tension test

The static tension test was carried out to obtain basic mechanical properties of the five structural steels. A total of 15 smooth specimens were manufactured as shown in Fig.1(a), with 3 specimens for each group of steel grade as shown in Fig.1(b). The main chemical composition of each steel was shown in Table 1. The tension test was conducted on a testing machine of WDW-100 at room temperature as shown in Fig.1(c) and data were collected by an extensometer attached to it. A displacement rate of 10mm/min was exerted on each specimen continuously until the specimen was totally fractured. The material properties including the yield strength σ_y, tensile strength σ_u and elastic modulus E of each specimen was listed in Table 2 and their averages over each group were also listed.

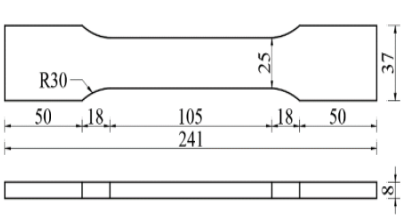

(a) Specimen plain figuration (Unit: mm)

(b) Manufactured specimens

(c) Specimen clamping

Fig. 1 Static tension test

Table 1
Chemical composition of each steel (%)

Steel	C	Si	Mn	P	S	Cr	Ni	Cu
Q235B	0.17	0.17	0.26	0.02	0.015	0.03	0.03	0.01
Q355B	0.21	0.14	0.42	0.022	0.01	0.03	0.02	0.01
Q460C	0.08	0.12	1.45	0.014	0.003	0.031	0.012	0.031
Q550D	0.079	0.17	1.05	0.016	0.003	0.041	0.019	0.020
Q690D	0.15	0.21	1.30	0.015	0.004	0.227	0.009	0.011

Table 2
Static tenstion test results

Steel	σ_y (MPa)	σ_u (MPa)	E (GPa)	Steel	σ_y(MPa)	σ_u (MPa)	E (GPa)
Q235B-1	313.00	447.00	180.12	Q460C-3	470.00	575.00	166.54
Q235B-2	329.00	448.00	176.54	**Q460C Avg**	**472.03**	**581.37**	**180.05**
Q235B-3	322.00	441.00	180.34	Q550D-1	622.00	692.00	185.09
Q235B Avg	**321.33**	**445.33**	**179.00**	Q550D-2	655.00	710.00	180.82
Q355B-1	473.00	583.00	183.42	Q550D-3	636.00	706.00	186.5
Q355B-2	473.00	591.00	180.30	**Q550D Avg**	**637.67**	**702.67**	**184.14**
Q355B-3	460.00	576.00	182.10	Q690D-1	707.00	755.00	194.2
Q355B Avg	**468.67**	**583.33**	**181.94**	Q690D-2	702.00	755.00	167.65
Q460C-1	474.10	582.10	184.9	Q690D-3	705.00	755.00	202.1
Q460C-2	472.00	587.00	188.71	**Q690D Avg**	**704.67**	**755.00**	**187.98**

It is found from Table 2 that mechanical properties of each steel in the specimens meet the requrement proposed by GB 55006-2021[16]. Three indexes including yield strengths, tensile strengths and elastic modulus all generally increase with the steel grade. It is worth noting that all three Q355B specimens are with rather high yield strengths and tensile strengths, which almost overtook those of Q460C specimens. It may mainly stem from the mechanical difference between various steel batches, since only the minumum values instead of maximun values of the yield strength and tensile strength are ruled in GB 55006-2021 and this batch of Q355B certainly meet the demands proposed in this code.

3. Fatigue crack growth rate test

The CT specimen designed according to GB/T 6398-2017[17] was shown in Fig.2(a) and it was with an initial notch with a length of a_{ini}=9+3.75=12.75mm from the center of the bolt. Two specimens were manufactured each for Q235B and Q355B and four specimens were manufactured each for three high-strength steels. The fatigue crack growth rate test was conducted on a fatigue testing machine PWS-100 in room temperature and the clamping of these specimens were shown in Fig.2(b). The crack length was observed with the help of a scale ruler attached to the specimen surface and an electron microscope placed in front of the testing machine. A crack with a length of 5.75mm was first prefabricated further based on the initial notch length of 12.75mm for each specimen by the exertion of sinusoid cyclic loading with a maximum value of F_{max}=37kN, a stress ratio of R=0.1 and a loading frequency of 30Hz. The fatigue crack growth test was subsequently started from a crack length of 5.75+12.75=18.5mm by the exertion of cyclic loading with the same loading as those in the prefabrication stage. The crack length a and the number of cycles N were both recorded at certain crack growth increments until the specimen was fractured with a sharp increase in the relative displacement between the two clamping ends. The failure mode of the specimen Q550D-1 was shown in Fig. 2(c). It is found that the section is clearly divided into several areas: the prefabricated notch, the crack initiation zone, the crack growth zone and the fracture zone. The crack initiation zone is located near the prefabricated notch tip with dark color and smooth section surface. The section surface gets rougher in the crack growth zone characterized by a stable crack growth. The fracture zone undergoes unstable fracture as soon as the crack reaches a critical length. The section surface gets rougher with plastic deformation and the crack grows in more irregular directions, which is similar to the characteristics of a static tension failure mode.

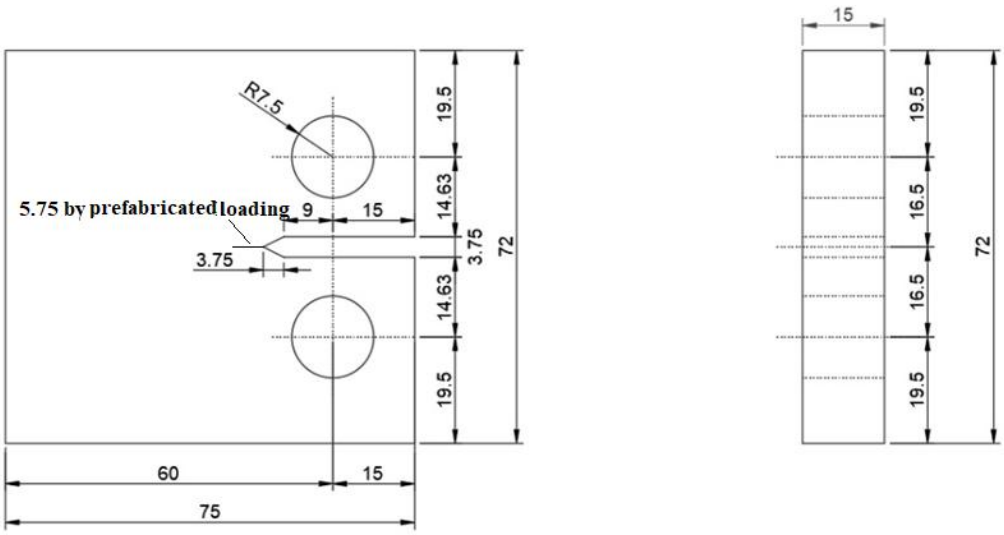

(a)Design of the specimen (Unit: mm)

(b) Clamping of the specimen

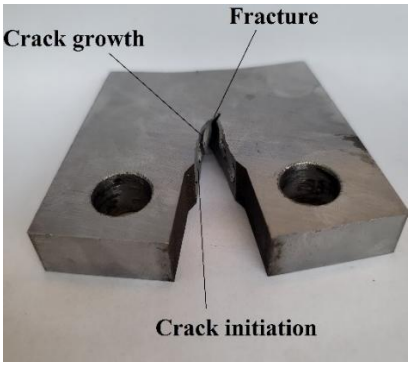

(c) Specimen of Q550D-1 after failure

Fig. 2 Fatigue crack growth rate test

The SIF K in a CT specimen is calculated according to Eq.(1) [17][18]:

$$K = \frac{F}{TW^{0.5}} g\left(\frac{a}{W}\right) \tag{1}$$

where a is the crack length; F is the loading force; T is the plate thickness and it is 15mm; W is the horizontal distance between the action line of the axial force and the far end of the specimen and it is 60mm; $g(a/W)$ is a shaping factor and it is calculated by Eq.(2)(3):

$$g\left(\frac{a}{W}\right) = \frac{(2+\alpha)\left(0.886+4.64\alpha-13.32\alpha^2+14.71\alpha^3-5.6\alpha^4\right)}{(1-\alpha)^{1.5}} \tag{2}$$

$$\alpha = \frac{a}{W},\ 0.2 \le \frac{a}{W} \le 1.0 \tag{3}$$

4. FE analysis

The FE analysis model of the CT specimen was established in the software ANSYS using the eight-node quadratic plane element named PLANE183 as shown in Fig.3(a). The mechanical properties of each steel in Table 2 were adopted in the analysis. Two uniform rows of sector elements were established around the crack tip and each row contained 18 sector elements (each with a sector angle of 10°) with a radius of r=0.1mm, as shown in Fig.3(b). The inner row of elements was simulated by modified PLANE183 with the mid-nodes skewed to the 1/4 point. The mesh size got sparser to 1mm gradually for regions away from the crack tip to save computing cost. A distributed force was applied to the nodes on the upper semicircle of the bolt hole to simulate the force by bolt.

The SIF K was calculated in ANSYS and only the results for typical crack lengths in the specimen Q550D-1 under F_{max}=37kN were given in Table 3 due to limitation on pages while other specimens showed the similar trend. The error, denoted as Er, between the FE analysis result $K_{max\text{-}fem}$ and the empirical solution $K_{max\text{-}solu}$ calculated by Eq.(1) were also listed.

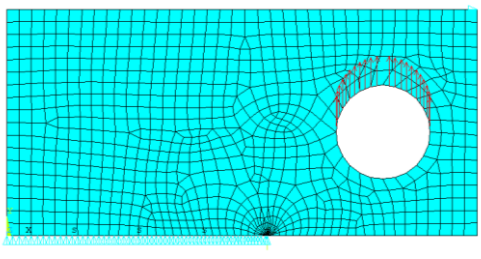

(a) Finite element model

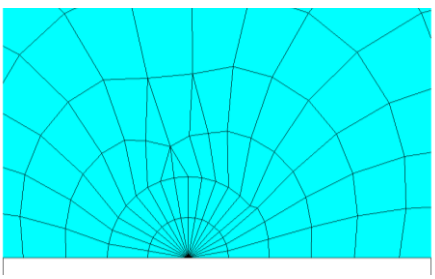

(b) Local meshing

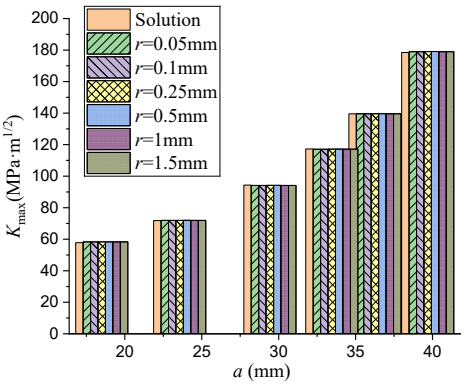

(c) SIFs under crack lengths

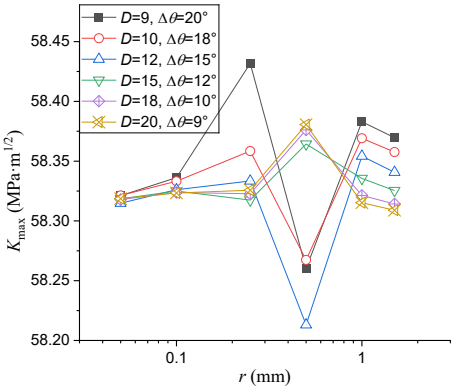

(d) SIFs using different mesh sizes

Fig. 3 Finite element analysis results

Table 3
Comparison of SIF results

a (mm)	$K_{max\text{-}solu}$ (MPa·m$^{1/2}$)	$K_{max\text{-}fem}$ (MPa·m$^{1/2}$)	Er	a (mm)	$K_{max\text{-}solu}$ (MPa·m$^{1/2}$)	$K_{max\text{-}fem}$ (MPa·m$^{1/2}$)	Er
18.5	57.782	58.302	0.90%	33.454	117.252	117.116	0.12%
23.566	71.831	71.959	0.18%	36.258	139.517	139.59	0.05%
29.428	94.332	94.142	0.20%	39.689	178.468	178.969	0.28%

It is found from Table 3 that the SIFs under different crack length obtained by FE analysis and empirical solution agree well with each other with an error less than 0.5%, which proves that the results by FE analysis are with sufficient accuracy. The mesh sensitivity check is indispensable for the SIF results around the crack tip since they are highly sensitive to the nearby mesh size. The number of the first row of sector elements around the crack tip D was fixed at 18 with a sector angle of 10° and the sector radius was changed into r=0.05mm, 0.1mm, 0.25mm, 0.5mm, 1mm and 1.5mm respectively for FE models with each crack length in Table 3. It is worth noting that the mesh size for the region away from the crack tip kept 0.5mm for the previous four radius conditions while it increased to 1mm for the latter two radius conditions to obtain high-quality meshing. The SIF results with various crack length and sector radius were illustrated in Fig.3(c). It is found that those results agree well with each other and all are close to the empirical solutions. It demonstrates that the crack length has little effect on the difference between SIFs obtained with different mesh size. Subsequently, the model with a crack length of a=18.5mm was selected and the number of the first row of sector elements around the crack tip D was change into 9, 10, 12, 15, 18 and 20 (the sector angle $\Delta\theta$ was 20°, 18°, 15°, 12°, 10° and 9°) while the sector radius r was also changed into 0.05mm, 0.1mm, 0.25mm, 0.5mm, 1mm and 1.5mm respectively. The change of SIF results with sector number D and sector radius r were illustrated in Fig.3(d) with a logarithmic coordinate in x-axis. It is found that the SIF gradually decreases and the discrepancy between each result also decreases with the increase in the sector element number D in general. The results of the models with $D \leq 12$ is relatively away from those with $D \geq 15$ for both r=0.25mm and 0.5mm while those with $D \leq 12$ were quite near to those with $D \geq 15$ for other four sector radius conditions. Thus, it is clear that the sector number D should be no less than 15 to get rather accurate results under each radius condition; Furthermore, the SIF results show a trend of decreasing after the first stage of increasing and it finally began to converge when $D \geq 15$. It should be noted that there is a negligible discrepancy rate of around 0.1% between the results with r=0.5mm or r=1mm and those with other four radius conditions, which may result from the difference in mesh sizes away from the crack tip. Therefore, it is concluded from the above analysis that rather accurate results can be obtained with a sector radius of r=1mm and a sector number of D=15 in this FE model.

5. DIC analysis

Comparison of results obtained by DIC analysis and FE analysis needs to be made to verify the accuracy of the test results. DIC is a non-contact measurement method which can calculate the full-field displacements and strains of the observed object. High-contrast and high-density speckle is required on the surface of the object and the images of the object are captured by a HD camera with the help of reliable light source for a 2D DIC analysis. The selected section of images captured called subsets are analyzed based on advanced algorithms which measure displacements of points by correlation between reference subsets before deformation and deformed subsets after deformation, as shown in Fig.4(a). For example, the reference subset before the deformation with a center point P (x, y) becomes the deformed subset with a center point P' (x', y') after the deformation, with a horizontal displacement of u and a vertical displacement of v as shown in Fig.4(b). To get all the information of correlation between the reference subset and the deformed subset, some certain neighboring points (pixels) need to be analyzed. Take the point Q (x+Δx, y+Δy) which becomes Q' (x'+$\Delta x'$, y'+$\Delta y'$) after the deformation for example, the coordinates of it meet Eq.(4) and Eq.(5)[19]:

$$x' + \Delta x' = x + u(P) + \frac{\partial u(P)}{\partial x}\Delta x + \frac{\partial u(P)}{\partial y}\Delta y + \Delta x \tag{4}$$

$$y' + \Delta y' = y + v(P) + \frac{\partial v(P)}{\partial x}\Delta x + \frac{\partial v(P)}{\partial y}\Delta y + \Delta y \tag{5}$$

The unknown horizontal and vertical displacements along with their gradients in the equations are optimized with the best correlation between the subsets for all the pixels. After the correlation, the displacement of discretized subsets of the whole image is tracked and thus the displacement vectors and strain field of the object are further obtained.

Two CT specimens made of GB Q355B were selected to conduct the fatigue test with 2D-DIC analysis. One lateral surface of the specimen was evenly sprayed with matte white paint and black paint to form sharp-contrast and high-density speckles with a size around 0.3mm-0.6mm, as shown in Fig. 4(c). The camera was set firmly on a tripod and the light source was placed at a proper distance from the specimen to keep adequate illumination as shown in Fig.4(d). The full-length video of the test for the specimen was recorded by a high-definition camera with a resolution of 1920×1080 pixels and an FPS of 60. Regarding to the image scale calibration, it was observed that one pixel approximately corresponded to a spatial area of 0.0786 × 0.0786 mm^2 on the object.

As a non-contact measurement method, DIC is inevitably with errors during the test. There are normally two types of errors in DIC analysis: bias errors and variance errors. Bias errors refer to an offset of the mean from the true value while variance errors refer to random errors centered with the mean about the true value. The following main errors during the test were considered and the measures to mitigate them were taken:

(1) Lens distortion. Lens distortion results in some kind of deformation of images, which brings bias error to DIC results. To minimize the effect of lens distortion, the focal length of the camera was adjusted to make the FOV approximately the same size as the specimen in Fig.4(c) and thus the crack to be observed was positioned in the center of the frame where lens distortion was least noticeable.

(2) Out-of-plane motion. This is a main source of bias errors for 2D DIC analysis. The motion of the specimen should be completely parallel to the lens since out-of-plane motion (motion vertical to the lens) brings bias errors to the test. During the calibration stage, the distance of four specimen corners to the

lens was carefully measured and checked to make sure the specimen surface was parallel to the lens. Both the camera and the specimen were carefully adjusted in such a way that the loading and reactions act in the plane of the specimen.

(3) Vibration during the test. There are two types of vibration involved during the test, which are the camera vibration and the specimen vibration. The camera vibration was far smaller than the specimen vibration. As mentioned above, the camera was placed firmly on a tripod and some foam boards were placed between the tripod and ground to avoid potential ground vibration induced by the test machine vibration. The specimen vibration was relatively large and difficult to mitigate. The frequency of the cyclic loading during the fatigue test in DIC analysis was reduced to 2Hz to decrease the effect of the specimen vibration.

(4) Limitation of the camera. The camera was with an FPS of only 60. As mentioned above, the frequency of the cyclic loading during the fatigue test in DIC analysis was adjusted to 2Hz to enhance the accuracy of the video capture and thus there were 30 images for one full cycle. Before the test, the camera was turned on to warm up to a stable working temperature.

To verify the effect of the above error sources, a motionless test was conducted on the two specimens in advance before the crack prefabrication to estimate the accuracy of the DIC system. No loading or deformation was applied on the CT specimens and thus the results including vertical displacement of the notch tip u_y and the strain in the vertical direction ε_y at the notch should ideally be zero. The variation of u_y and ε_y within recorded images was illustrated in Fig.4(e)(f). It is found that both the displacement and the strain fluctuated within these images, and the strain data fell into a more intensive region than the displacement data, since some strain data of the two specimens overlapped each other. The distribution of u_y and ε_y was additionally illustrated in Fig.4(g)(h). It is found that both the displacement and the strain within two specimens demonstrated normal distribution. The mean value *mu* of the vertical displacement is around ±1μm and that of the strain is around ±0.005% (5×10^{-5}), which represents the bias error while the variance $sigma^2$ represents the variance error. Fig.4(h) demonstrates that the variation of ε_y is within ±0.03% ($\pm3\times10^{-4}$), which is far smaller than the vertical strain ε_y in the following fatigue test. Therefore, it is concluded that the above-mentioned errors are relatively small and can be ignored. It is worth noting that the error resulted from vibration during the test cannot be taken into account in the motionless test since the motionless test can only consider the errors in a static condition. However, the results obtained by FE analysis and DIC analysis will be compared in the following paragraph to verify the accuracy of the DIC analysis results.

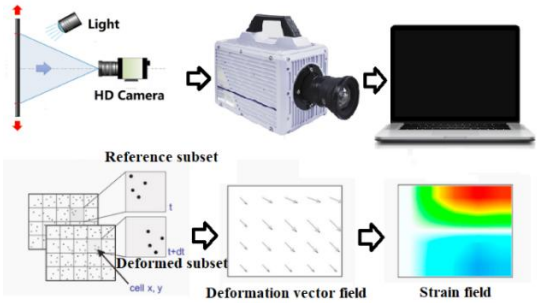

(a) DIC fundamentals

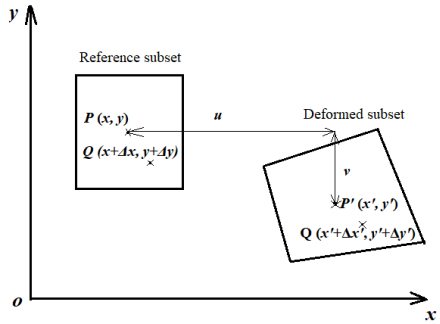

(b) Deformation of subset

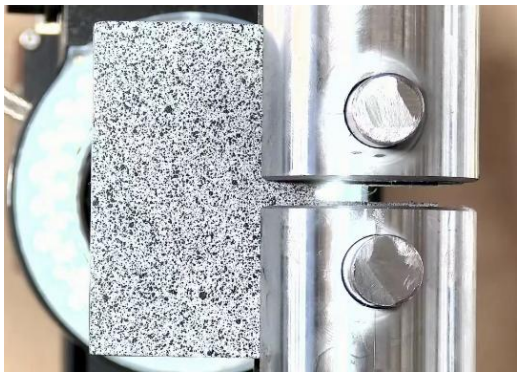

(c) Speckle on the specimen surface

(d) DIC system setup

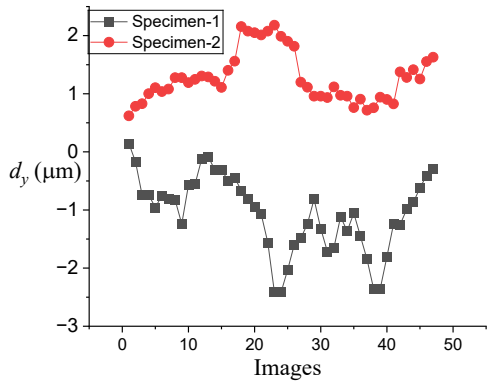

(e) Motionless test displacement with images

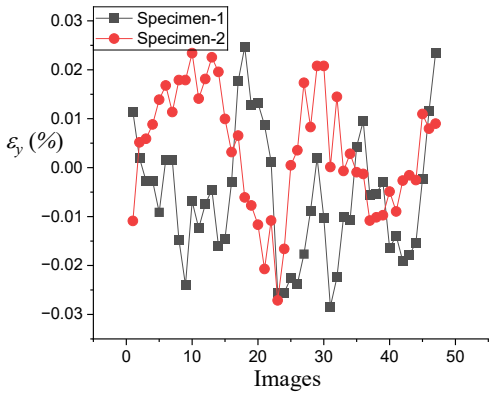

(f) Motionless test strain with images

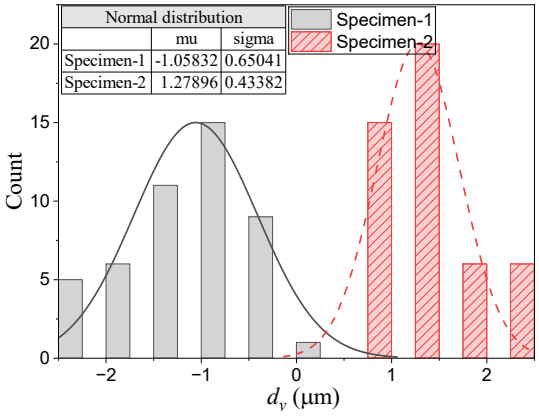

(g) Motionless test displacement distribution

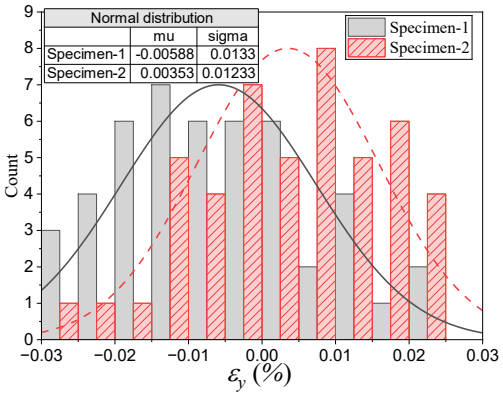

(h) Motionless test strain distribution

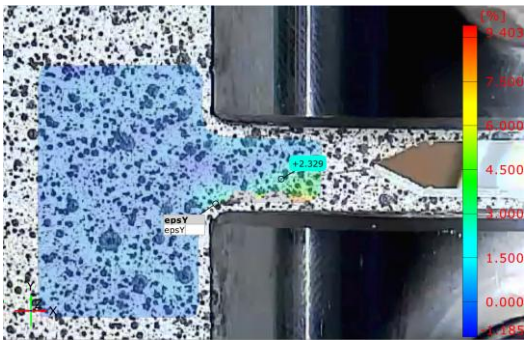

(i) Strain contour of ε_y by DIC for Specimen 1 with a=19.574mm (Unit: %)

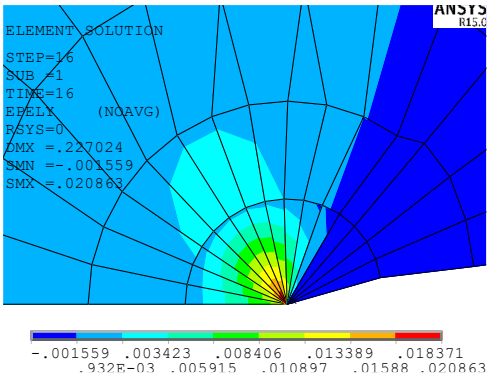

(j) Strain contour of ε_y by FE analysis for Specimen 1 with a=19.574mm (Dimensionless quantity)

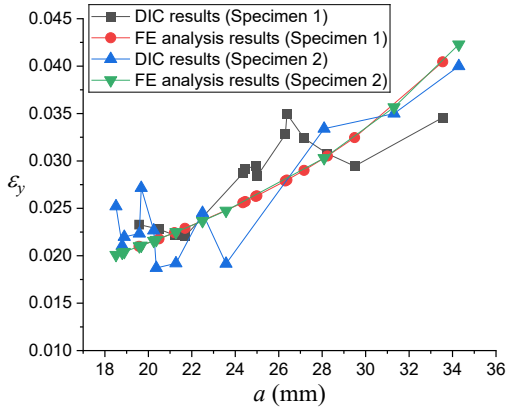

(k) Local strain comparison for DIC and FE analysis

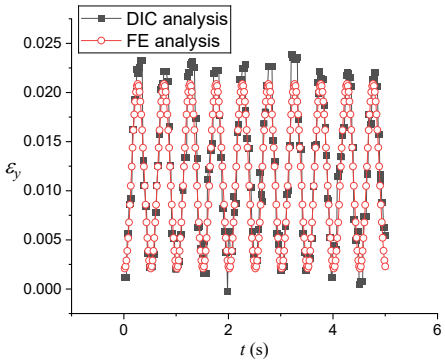

(l) Comparison of local strain time-history for DIC and FE analysis (Specimen 1with a=19.574mm)

Fig. 4 DIC analysis

The prefabrication of the crack was further conducted for these two specimens with the same loading described in Section 4 while the frequency of the cyclic loading was reduced to 2Hz. The videos were further analyzed in the DIC-processing software GOM Correlate. Due to the limitation on pages, only the contour map of the maximum strain within one cycle in the vertical direction (Y-axis direction) ε_y around the crack tip for Specimen 1 with a certain crack length was illustrated in Fig.4(i) and that obtained by FE analysis with the same crack length was illustrated in Fig.4(j). The figure reveals that the strain distribution near the crack tip by DIC analysis generally agrees well with that by FE analysis. All the ε_y values around the crack tip in each crack increment were illustrated in Fig.4(k) to fully compare all the strain data. It is found that most strain data near the crack tip calculated by DIC analysis and by FE analysis agree well with each other, since the discrepancy rate between them for all strain data were within or around 20%, with a maximum of 22% and a minimum of 1%. The comparison of the strain time history near the crack tip for DIC analysis and FE analysis needs to be presented, for the strain was fluctuating during the test. Due to the limitation on pages, only the strain time history in Specimen 1 with a crack length of 19.574mm was illustrated in Fig.4(l) and others showed similar trends. It is found that the strain by these two types of analysis both fluctuate synchronously with the time, with a uniform frequency of 2Hz and a maximum discrepancy rate below 10%. Therefore, it proves the fact that the results obtained by DIC analysis agree well with those by FE analysis and the test results are sufficiently accurate, even with the error resulted from vibration during the test.

6. Fatigue cack growth rate data analysis

Paris law based on the SIF range is shown in Eq.(6):

$$da/dN = C(\Delta K)^m \tag{6}$$

Where N is the number of cycles; da/dN is the crack growth rate; ΔK is the SIF range; C and m are material-dependent constants. Take logarithms on both sides in Eq.(6) to get the linear equation of Eq.(7) and the constants of C and m are obtained through linear fitting of fatigue test data.

$$lg\frac{da}{dN} = lgC + mlg\Delta K \tag{7}$$

SEDF S is defined by the multiplication of total strain energy stored per unit volume with a specific critical distance r away from the point of singularity at the crack tip, as shown in Eq.(8):

$$S = \omega \cdot r = \lim_{\Delta V=0} \frac{\Delta W_t}{\Delta V} \cdot r = \frac{dW_t}{dV} \cdot r \tag{8}$$

where ΔW_t is the total strain energy within a volume of ΔV, thus leading to a strain energy density ω. The use of SEDF is able to determine not only the crack growth rate but also the crack growth direction from its minimum value around the crack tip[20]. The relation of it with SIF in a mode I crack K_I is shown as Eq.(9), while other crack modes are not discussed due to limitation on pages.

$$S = a_{11} K_I^2 \tag{9}$$

$$a_{11} = \frac{1}{16\pi G}(1 + cos\theta)(\kappa - cos\theta) \tag{10}$$

$$G = E/2(1 + \upsilon) \tag{11}$$

$$\kappa = \begin{cases} 3 - 4\upsilon, & \text{plain strain} \\ (3 - \upsilon)/(1 + \upsilon), & \text{plain stress} \end{cases} \tag{12}$$

where a_{11} and κ are coefficients calculated by Eq.(10) and Eq.(12); G is the shear modulus calculated by Eq.(11); υ is the Poisson's ratio; θ is the angle in the polar coordinate around the crack tip. The crack growth rate da/dN is thus calculated by Eq.(13)[14][20]:

$$\frac{da}{dN} = A(\Delta S)^n \tag{13}$$

where ΔS is the SEDF range; A and n are material-dependent constants. The definition of these two constants for each material requires numerous fatigue crack growth tests, similar to Paris law. The use of SEDF in fatigue crack growth analysis is rather limited due to the lack of related test data, which is considered as the most vital shortcoming in this method. It is worth noting that the SEDF range ΔS is deduced into Eq.(14) according to Eq.(9):

$$\Delta S = a_{11}(K_{Imax}^2 - K_{Imin}^2) = 2a_{11}\overline{K}_I \Delta K_I = a_{11}(1 - R^2)K_{Imax}^2 \tag{14}$$

where $\overline{K}_I$ is the mean value of K_I. It is found from Eq.(14) that the use of SEDF range is able to consider the effect stress ratio by the use of mean stress[20]. Eq.(13) is further deduced into the linear equation of Eq.(15) to get a linear relation.

$$lg\frac{da}{dN} = lgA + nlg\Delta S \tag{15}$$

It has been proved that the use of SEDF is able to obtain both rather accurate fatigue crack growth rate results and crack growth direction results[20-23]. Unfortunately, the direct comparison of prediction accuracy between these two methods when dealing with fatigue crack growth is rarely reported in current literature. Choi et al.[22][23] applied both SEDF method and Pris law to fatigue crack growth analysis of in-plane and out-of-plane gusset welded joints to obtain the material constants data while they conducted the crack growth prediction only based on SEDF method; Sih and Tang[24] demonstrated the use of both methods simultaneously in the assurance of reliable time limits in fatigue with reliability analysis while the conclusion cannot be applied to fatigue crack growth test analysis. The above comparison is summarized in Table 4.

Table 4
Comparison of SIF and SEDF methods

	Paris law	Equation based on SEDF
Key index	SIF	SEDF
Key index purpose	To describe the severity of the stress distribution around the crack tip	
Method based on	Stress and strain	Energy
Applicability	Crack growth rate analysis	Crack growth rate & direction analysis
Consider stress ratio	Unable, unless a modification is used	Able
Test data sources	Wide	Limited
Prediction effect	Accurate	

Based on the above knowledge, the fatigue test data were processed by secant method as shown in Eq.(16)[18]:

$$(da/dN)_{\bar{a}} = (a_{i+1} - a_i)/(N_{i+1} - N_i) \tag{16}$$

where $(da/dN)_{\bar{a}}$ is the average crack growth rate over the increment of $(a_{i+1} - a_i)$; The SIF range ΔK and the SEDF range ΔS within each increment is calculated using the average crack length $(a_{i+1} + a_i)/2$.

The relation between the crack length a and the number of cycles N recorded during the crack growth of all specimens was plotted in Fig.5(a), where the crack growth rate (da/dN) is indicated by the slope of each curve. It is found from the figure that the crack growth rates of various steels gradually decrease with the increase of the yield strength and however the trend is not strictly followed. For example, discreteness is found in the a-N curves of Q550D, where the curves of Q550D-1 and Q550D-2 are close to each other with a growth rate even lower than that of all specimens of Q690D, while the curves of Q550D-3 and Q550D-4 are close to each other which fall between those of Q460C and Q690D. This discreteness may be due to the difference in steel batches and randomness in manufacture. It has also been noted by Tong et al[3] that there are some differences in the crack growth test results of different batches of steel plates even with similar strength. It is worth noting that the crack growth rate of the two specimens of Q355B in this test is even slower than that of Q460C due to the fact that they generally share similar yield strengths as listed in Table 2.

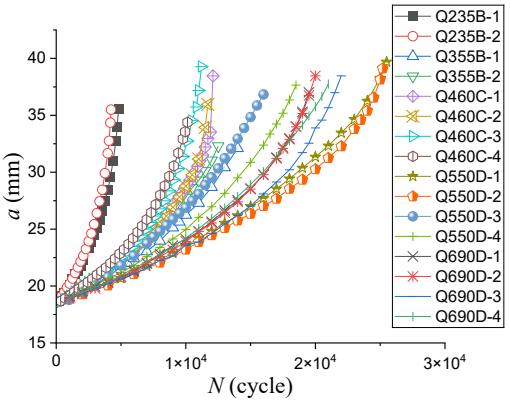

(a) a-N curve

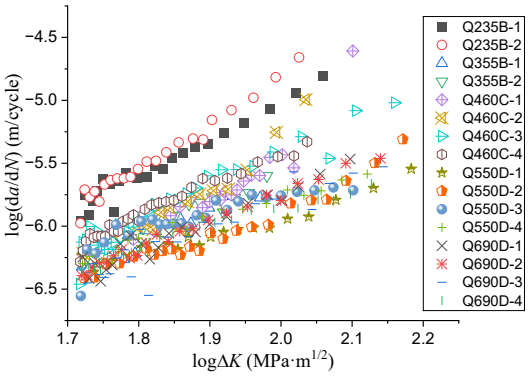

(b) Log(da/dN)-logΔK curve by single specimen

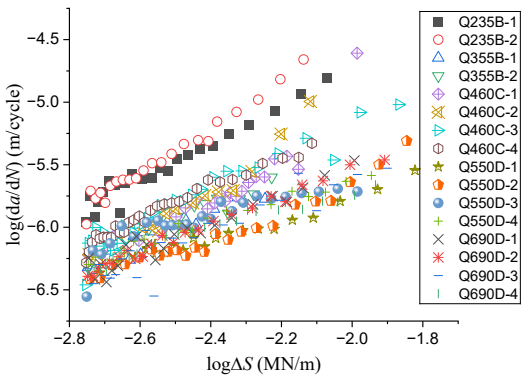

(c) Log(*da*/*dN*)-logΔS curve by single specimen

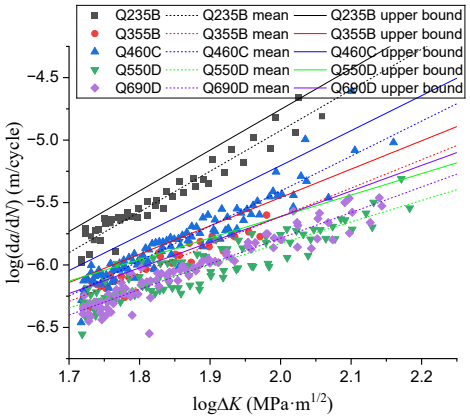

(d) Log(*da*/*dN*)-logΔK curve by specimen groups

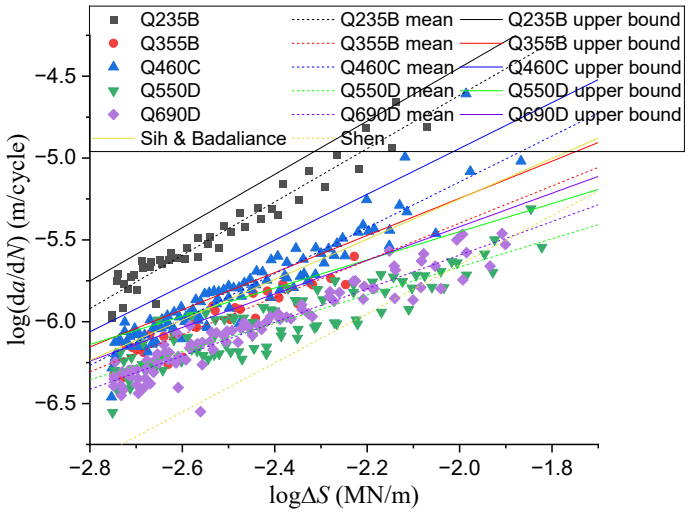

(e) Log(*da*/*dN*)-logΔS curve by specimen groups

Fig. 5 Test data analysis

Table 5
Fitting results of specimens

Specimen	Paris law by SIF range (Unit: da/dN-m/cycle, ΔK-MPa·m$^{1/2}$)				Crack growth rate equation by SEDF range (Unit: da/dN-m/cycle, ΔS-MN/m)			
	m	log$C$	C	R_1^2	n	log$A$	A	R_2^2
Q235B-1	2.978	-10.966	1.081×10^{-11}	0.948	1.489	-1.753	1.766×10^{-2}	0.948
Q235B-2	3.635	-12.087	8.185×10^{-13}	0.973	1.818	-0.838	1.452×10^{-1}	0.973
Average	**3.307**	**-11.526**	**2.979×10^{-12}**	**0.961**	**1.653**	**-1.296**	**5.058×10^{-2}**	**0.961**
Group	**3.258**	**-11.439**	**3.639×10^{-12}**	**0.935**	**1.629**	**-1.359**	**4.375×10^{-2}**	**0.935**
Q355B-1	2.243	-10.129	7.430×10^{-11}	0.811	1.122	-3.189	6.471×10^{-4}	0.811
Q355B-2	2.197	-9.989	1.026×10^{-10}	0.911	1.098	-3.193	6.412×10^{-4}	0.911
Average	**2.220**	**-10.059**	**8.730×10^{-11}**	**0.861**	**1.110**	**-3.191**	**6.442×10^{-4}**	**0.861**
Group	**2.270**	**-10.151**	**7.063×10^{-11}**	**0.857**	**1.135**	**-3.128**	**7.447×10^{-4}**	**0.857**
Q460C-1	3.057	-11.534	2.924×10^{-12}	0.839	1.528	-2.077	8.375×10^{-3}	0.839
Q460C-2	3.407	-12.140	7.244×10^{-13}	0.906	1.704	-1.597	2.529×10^{-2}	0.906
Q460C-3	2.728	-10.867	1.358×10^{-11}	0.931	1.364	-2.426	3.750×10^{-3}	0.931
Q460C-4	2.591	-10.592	2.559×10^{-11}	0.966	1.295	-2.577	2.649×10^{-3}	0.966
Average	**2.946**	**-11.283**	**5.212×10^{-12}**	**0.911**	**1.473**	**-2.169**	**6.776×10^{-3}**	**0.911**
Group	**2.800**	**-11.008**	**9.817×10^{-12}**	**0.894**	**1.400**	**-2.345**	**4.519×10^{-3}**	**0.895**
Q550D-1	1.593	-9.108	7.798×10^{-10}	0.958	0.796	-4.180	6.607×10^{-5}	0.958
Q550D-2	2.153	-10.159	6.934×10^{-11}	0.942	1.077	-3.496	3.192×10^{-4}	0.942
Q550D-3	1.571	-8.897	1.268×10^{-9}	0.768	0.785	-4.037	9.183×10^{-5}	0.736
Q550D-4	1.789	-9.354	4.426×10^{-10}	0.969	0.894	-3.819	1.517×10^{-4}	0.969
Average	**1.776**	**-9.379**	**4.178×10^{-10}**	**0.909**	**0.888**	**-3.883**	**1.309×10^{-4}**	**0.901**
Group	**1.721**	**-9.270**	**5.370×10^{-10}**	**0.803**	**0.861**	**-3.944**	**1.138×10^{-4}**	**0.803**

Q690D-1	2.286	-10.301	5.000×10^{-11}	0.931	1.143	-3.230	5.888×10^{-4}	0.931
Q690D-2	2.233	-10.202	6.281×10^{-11}	0.986	1.116	-3.295	5.070×10^{-4}	0.986
Q690D-3	2.179	-10.155	1.081×10^{-11}	0.854	1.089	-3.414	1.766×10^{-2}	0.986
Q690D-4	1.591	-9.042	8.185×10^{-13}	0.961	0.796	-4.119	1.452×10^{-1}	0.961
Average	**2.072**	**-9.925**	**2.979×10^{-12}**	**0.933**	**1.048**	**-3.470**	**5.058×10^{-2}**	**0.909**
Group	**2.051**	**-9.888**	**3.639×10^{-12}**	**0.902**	**1.026**	**-3.542**	**4.375×10^{-2}**	**0.902**

The relations between the logarithm of the crack growth rate da/dN and the SIF range ΔK or the SEDF range ΔS for each single specimen were illustrated in Fig.5(b)(c) and a nearly linear correlation is found for each specimen. Additionally, the above relations for each group of the same steel were plotted as shown in Fig.5(d)(e). The crack growth constants m, log$C$, n and log$A$ were obtained by fitting using the test data in each single specimen or in specimen groups respectively based on Eq.(7) and Eq.(15). The results along with the average constants over each group were listed in Table 5. The coefficients of determination R_1^2 and R_2^2 for SIF method and SEDF method were given respectively.

It is found from Table 5 that with the increase of the yield strength, m and n both show a generally gradual decreasing trend while the absolute value of log$C$ and log$A$ gradually decreases and increases respectively, with the straight lines gradually moving down in Fig.5(b)-(e), although the trend is not strictly followed. Based on the comparison between the average fitting results over each single specimen and the direct fitting results by specimen group, it is found that they are relatively close to each other with a difference rate less than 5%, which reveals that either method leads to accurate results. It is also found that the coefficient of determination for most specimens are higher than 0.9 although they get slightly lower to around 0.8 in some specimens due to uncertainties, which indicates that linear correlation exists between both lg(da/dN) and lg(ΔK), or lg(da/dN) and lg(ΔS), with generally good fitting effect.

7. Test results comparison and guidance to design

The crack growth test results of high-strength steel CT specimens based on the SIF range ΔK in related literatures were fully summarized in Table 6 and plotted in Fig.6(a). It is found that the straight line of each test result generally moves downward with the increase in the yield strength, indicating a slower crack growth rate, however, which is not strictly followed. Moreover, it is found that the crack growth rate constants of the same steel in this test and in related literatures are relatively close to each other with consistency, which verifies the reasonability of the results obtained in this test. However, there are few crack growth rate test data of structural steel based on SEDF. The limited data from two relevant literatures were listed in Table 7 and represented in Fig.5(e). It is found that the constants obtained in this test is in good agreement with those in these two literatures.

Although it has been reported that scatter of fatigue crack growth of visible cracks is generally lower than that of fatigue crack iniatiaion[36], Table 5 still reveals some sort of uncertainties leading to test result scatter. In general, uncertainties may stem from a wide range of sources including material inhomogeneity, batch differences, specimen production differences, specimen surface quality differences, specimen variability, test load errors, laboratory environment variation, etc. These uncertainties are normally considered by statistical analysis of test data.

The test data for each steel were processed in material groups based on the assumption of a normal distribution in variables. The upper bound for the test data in each group was illustrated in Fig.5(d)(e), which represented a survival probability of α'=95% (5% probability of failure) with a one-sided confidence level of γ=95% (corresponding to an actual survival probability of α=97.7%). The fitted constants for the upper bounds were all listed in Table 8. It is found that almost all the test data falls under the upper bound for each material as shown in Fig.5(d)(e). Each upper bound is considered as a specific design curve for each steel, since it meets the demand of a design curve with a survival probability of α=97.7%.

Table 6
Test constants in literatures based on ΔK (Unit: da/dN-m/cycle, ΔK-MPa·m$^{1/2}$)

Researcher	Steel grade	R	T(mm)	σ_y (MPa)	m	C	lg$C$
Zong et al. [9]	Q345qD	0.1	10.00	363	2.870	9.772×10^{-12}	-11.010
Liao et al. [25]	Q345qD	0.1	13.85	382	2.653	1.970×10^{-11}	-10.705
Tong et al. [3]	Q460C	0.1	10.00	481	2.460	4.140×10^{-11}	-10.383
Ma et al. [4]	Q550E	0.1	8.00	605	2.130	1.549×10^{-10}	-9.810
Tong et al. [3]	Q550D	0.1	10.00	704	2.644	1.530×10^{-11}	-10.816
Guo et al. [6]	Q690D	0.1	15.08	732	2.682	1.866×10^{-11}	-10.729
Tong et al. [3]	Q690D	0.1	10.00	801	1.928	1.920×10^{-10}	-9.718
Tan et al. [26]	Q690	0.1	15.00	≥690	2.215	6.890×10^{-11}	-10.162
Shen et al. [27]	EH690	0.1	12.70	797	2.720	1.090×10^{-11}	-10.963
Zong et al. [10]	Q690D	0.1	10	788	2.600	1.517×10^{-11}	-10.819
Chen et al. [12]	Q420C	0.1	12	430	3.090	4.080×10^{-12}	-11.389
Lukacs et al. [28]	S690QL	0.1	13	791	1.700	8.070×10^{-10}	-9.093
Wang et al. [29]	E690	0.1	2	≥690	2.999	3.531×10^{-12}	-11.452
Yang et al. [30]	Q420B	0.1	20	442	2.580	3.400×10^{-11}	-10.469
Wang et al. [31]	10Ni5CrMoV	0.1	5	811	1.926	2.701×10^{-10}	-9.568
Zhong et al. [32]	EH36	0.1	10	449	2.996	7.775×10^{-12}	-11.109
Duan et al. [33]	HPS 485W	0.1	7.5	≥485	2.840	1.050×10^{-11}	-10.979
Wang et al. [34]	HPS 485W	0.1	12.5	520	2.530	2.190×10^{-11}	-10.660
Song et al. [11]	10CrNi3MoV	0.1	8	710	2.650	1.240×10^{-11}	-10.907
Zong et al. [35]	WNQ570	0.1	10	495	2.800	3.981×10^{-12}	-11.400

Table 7
Test constants in literatures based on ΔS (Unit: da/dN-m/cycle, ΔS-MN/m)

Researcher	Steel grade	R	T(mm)	σ_y (MPa)	n	A	lg$A$
Sih [21] and Badaliance [14]	300M	-	-	1620	1.234	1.660×10^{-3}	-2.781
Shen [15]	Q235B	0.1	14.00	235	1.500	2.230×10^{-3}	-2.652

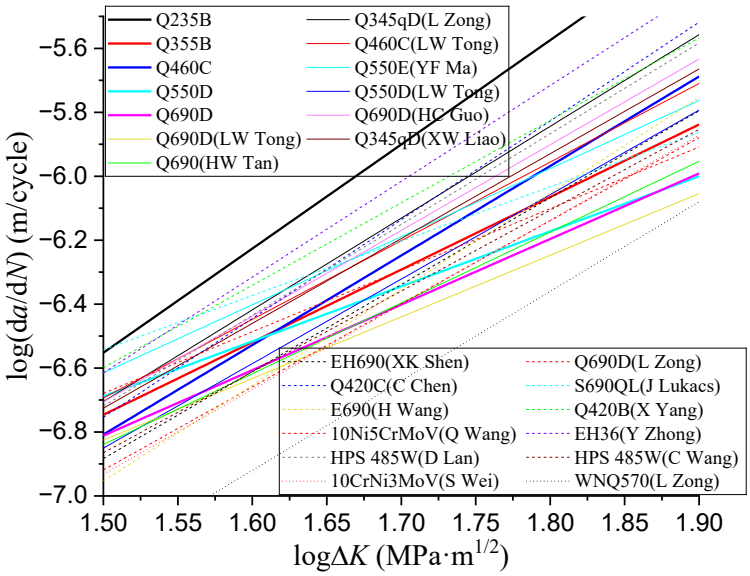

(a) Comparison with results in literatures

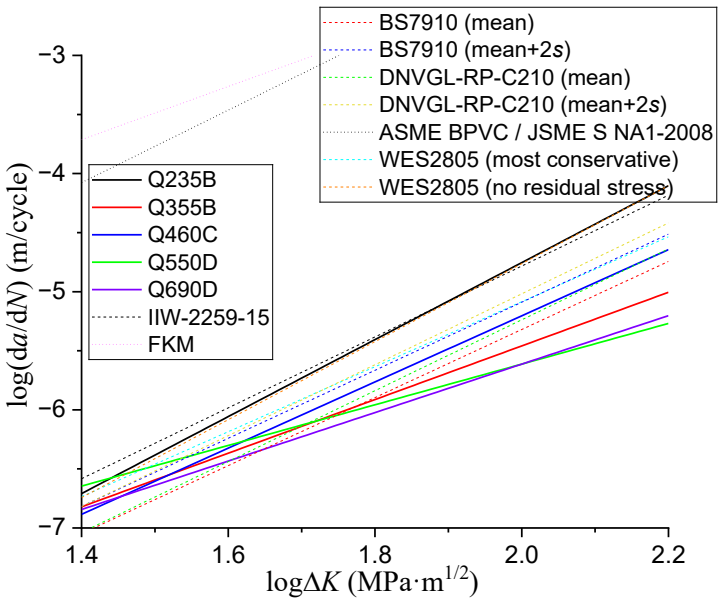

(b) Comparison with design curves

Fig. 6 Comparison of results

Table 8
Fitting results of specimens with α'=95% and γ=95% ($\alpha\approx97.7\%$)

Specimen	Paris law by SIF range (Unit: da/dN-m/cycle, ΔK-MPa·m$^{1/2}$)			Crack growth rate equation by SEDF range (Unit: da/dN-m/cycle, ΔS-MN/m)		
	m	log$C$	C	n	log$A$	A
Q235B	3.258	-11.270	5.369×10^{-12}	1.629	-1.191	6.446×10^{-2}
Q355B	2.270	-9.999	1.002×10^{-10}	1.135	-2.976	1.057×10^{-3}
Q460C	2.800	-10.804	1.570×10^{-11}	1.400	-2.140	7.237×10^{-3}
Q550D	1.721	-9.055	8.812×10^{-10}	0.861	-3.729	1.866×10^{-4}
Q690D	2.051	-9.715	1.926×10^{-10}	1.026	-3.369	4.279×10^{-4}

Several fatigue crack growth design curves based on Paris law have been proposed in design codes and standards. Some typical ones are listed in Table 9. It is worthwhile comparing the design curves in these codes with those upper bounds established in this study. It is worth noting that the comparison is based on the Paris law since SEDF method is adopted in none of these codes. The codes are briefly introduced as follows and the related constants are all listed in Table 9:

(1) IIW-2259-15[37] is the design code suggested by International Institute of Welding (IIW). Generally, it is a code for welded joints but it also gives the suggested crack growth curve constants for the base metal of common steel. The constants listed in Table 9 represent the upper bound with a survival probability α'=95% at a two-sided confidence level of the mean of γ=75% (corresponding to an actual survival probability of α=97.7%, i.e., mean minus two standard deviations 2s).

(2) BS7910 2019[38] is a standard issued by the British Standards Institution, which gives the suggested crack growth curve constants for common steel. It suggests two types of curves: a simplified curve for preliminary screening assessment and a precise two-stage curve for accurate assessment. The Stage b curve for the two-stage type was selected and its mean curve and the upper bound (α=97.7%, i.e., mean minus two standard deviations 2s) were listed respectively.

(3) DNVGL-RP-C210[39][40] is a fatigue design code for offshore steel structures issued by DNV. It also suggests the crack growth curve constants for common steel under air condition. It contains a mean curve and an upper bound curve (α=97.7%, i.e., mean minus two standard deviations 2s).

(4) FKM[41][42] is a German guideline for fracture evaluation. It gives the upper limit of scatter band of steels.

(5) WES2805[43] is the code for fusion welded joints issued by the Japan Welding Engineering Society. It gives two curves for common steel: a most conservative curve and a curve for cracks growing with no residual stress and a stress ratio of R=0.

(6) ASME BPVC[44] and JSME S NA1-2008[45] both gives the same crack growth curve constants for ferritic steel in air environment as shown in Eq.(17). The constants were thus calculated according to Eq.(17).

$$C = 3.78 \times 10^{-12} \cdot 25.72 \cdot (2.88 - R)^{-3.07} \quad (0 \le R < 1) \tag{17}$$

Table 9
Paris law constants in codes (Unit: da/dN-m/cycle, ΔK-MPa·m$^{1/2}$)

No.	Code	Material type	R	m	C	lg$C$
1	IIW-2259-15 (mean+2s, α=97.7%)	Steel	-	3.000	1.650×10^{-11}	-10.783
2	BS7910 2019 (mean)	Steel	<0.5	2.880	8.320×10^{-12}	-11.080
3	BS7910 2019 (mean+2s, α=97.7%)	Steel	<0.5	2.880	1.410×10^{-11}	-10.849
4	DNVGL-RP-C210 (mean)	Steel	-	3.000	5.790×10^{-12}	-11.238
5	DNVGL-RP-C210 (mean+2s, α=97.7%)	Steel	-	3.000	9.604×10^{-12}	-11.018
6	FKM	Steel	-	2.250	1.370×10^{-7}	-6.863
7	WES2805 (most conservative)	Steel	-	2.750	2.600×10^{-11}	-10.585
8	WES2805 (no residual stress and R=0)	Steel	0	3.300	4.340×10^{-12}	-11.363
9	ASME BPVC/ JSME S NA1-2008	Ferritic steel	0.1	3.070	4.213×10^{-9}	-8.375

All the curves were simultanously illustrated in Fig.6(b). It is found that the curve suggested by ASME BPVC 2007 and JSME S NA1-2008 for ferritic steel and that by FKM seem too conservative for all the steels in this study, since they are rather high above all the other curves in the figure. Other curves except these two seem rather close to each other. It is found that the upper bound of Q235B falls above the other upper bounds while IIW-2259-15 and WES2805 are barely enough to cover the upper bound of Q235B, which means these two design curves are applicable to the design of all the steels in this study. However, it must be kept in mind that the above analysis is based on the fact that there are only two specimens involved each for Q235B and Q355B, leading to a tremendous rise in the effect of uncertainty. The comparison of the other three high-strength steels is much simpler, since there are sufficient number of specimens. It is found that all the curves except BS7910 (mean) and DNVGL-RP-210 (mean) fall above the upper bounds of the three high-strength steels in most ranges of logΔK as shown in Fig.6(b). It demonstates that BS7910 (mean+2s), DNVGL-RP-210 (mean+2s), WES2805 and IIW-2259-15 are all applicable to the design of these three high-strength steels, while BS7910 (mean) and DNVGL-RP-210 (mean) are both not applicable due to the neglection of scatter upper bound.

It is worth noting that due to the low m value in Paris law for Q550D, most of the above design curves no longer cover the upper bound of Q550D when logΔK is approxmately smaller than 1.5 MPa·m$^{1/2}$. However, the fatigue crack growth rate analysis based on both SIF range and SEDF range is limited to the stable crack growth stage within which the crack growth rate da/dN is in a straight line with the SIF range ΔK or SEDF range ΔS in a log-log coordinate. The stable crack growth stage is with a growth rate approximately from 10^{-9} to 10^{-5} m/cycle, corresponding to a logΔK of 1.4-2.2 MPa·m$^{1/2}$ in the CT specimens while other ranges of logΔK is not necessary to discuss. Therefore, the above conclusion is still generally applicable to Q550D.

Therefore, each upper bound is applicable to the design of the specific high-strength steel. These upper bounds are considered as the fatigue crack growth design curves for each steel, which can be directly used for the fatigue crack growth rate analysis and design of cracked steel components or structures.

8. Conclusion

(1) The strain results at the crack tip of specimens obtained by FE analysis and DIC analysis are in good agreement with each other, indicating that both are useful tools for the verification of crack growth rate tests.

(2) The crack length has little effect on the difference between SIFs obtained by various mesh sizes while the SIF gradually converges as the angle and the radius of the first row of sector elements at the crack tip decrease in the FE analysis and rather accurate results can be obtained with a sector radius of r=1mm and a sector number of D=15 in this case.

(3) The crack growth rate gradually slows down, with the material constants m and n gradually decreasing and the absolute values of log$C$ and log$A$ gradually decreasing and increasing respectively, as the yield strength increases, although the trend is not strictly followed.

(4) The mean+2s curve in BS7910 and DNVGL-RP-210, along with the curves in WES2805 and IIW-2259-15 are all applicable to the design of Q460C, Q550D and Q690D, while the mean curve in BS7910 and DNVGL-RP-210 are not applicable, and the curves suggested by ASME BPVC or JSME S NA1-2008 for ferritic steel and that by FKM are too conservative.

(5) The scatter band upper bounds established for Q460C, Q550D and Q690D based on either SIF or SEDF with a survival probability 95% along with a one-sided confidence level 95% are able to be considered as design curves applicable to fatigue crack growth analysis and design of these three high-strength steels.

Acknowledgements

This research was supported by the National Natural Science Foundation of China (No.52008202).

Reference

[1] Barsom JM, Imhof EJ, & Rolfe ST . Fatigue-crack growth in high yield-strength steels[J]. Engineering Fracture Mechanics, 1971, 2(4): 301-317.
[2]Jesus DMA, Matos R, Fontoura FB, et al. A comparison of the fatigue behavior between S355 and S690 steel grades[J].Journal of Constructional Steel Research, 2012(79):140-150.
[3] Tong L, Ren Z, Jing S, et al., Experimental study of fatigue crack growth rate of high strength structural steel series[J], Engineering Mechanics, 2020, 37 (12): 191-201+212. (In Chinese)
[4] Ma YF, Cheng EX, Wu XS, et al. Fatigue crack growth of Q550E high strength steel and welded joint[J/OL]. Journal of Civil and Environmental Engineering:1-11[2024-06-07]. (In Chinese)
[5] Shen X ,Gao X ,Shao Y, et al. Investigation on the fatigue crack growth behavior of welded joints in EH690 high-strength marine steel[J].International Journal of Fatigue, 2024(189):108572.

[6] Guo H, Guan X, Pan Y, et al. Experimental research on fatigue crack growth behavior of Q690D high strength steel[J].Journal of Constructional Steel Research, 2024(220):108809.
[7] Panwitt H, Köster P, & Sander M. Fatigue crack growth determination under in-phase and out-of-phase mixed-mode loading conditions using an automated DIC evaluation tool[J]. International Journal of Fatigue, 2022(164): 107122.
[8] Li D, Huang P, Chen Z, et al. Experimental study on fracture and fatigue crack propagation processes in concrete based on DIC technology[J]. Engineering Fracture Mechanics, 2020(235):107166.
[9] Zong L, Shi G, Wang YQ, et al. Experimental study on fatigue crack growth rate of Q345qD bridge steel[J]. China Railway Science, 2015,36(03):37-44. (In Chinese)
[10] Zong L, Guo S, Liao X, et al. Experimental investigation on fatigue crack growth rate of Q690D high strength steel[J]. Journal of Building Structures, 2023, 44(8):217–24. (In Chinese)
[11] Song W, Wang P, Wan D, et al. Fatigue crack growth behavior of Ni-Cr-Mo-V steel welded joints considering strength mismatch effect[J]. International Journal of Fatigue, 2021(151): 106389.
[12] Chen C, Su M, Wang Y, et al. Experimental research on the fatigue crack growth behaviour of Q420C[J]. Journal of Constructional Steel Research, 2022(192):107241.
[13] Sih GC. Strain-energy-density factor applied to mixed mode crack problems[J]. International Journal of fracture, 1974, 10(3): 305-321.
[14] Badaliance R. Application of strain energy density factor to fatigue crack growth analysis[J]. Engineering Fracture Mechanics, 1980, 13(3): 657-666.
[15] Shen S. Research on fatigue property and life prediction of welding joints used in high-rise steel structures based on strain energy density[D]. Southeast University, 2019. (In Chinese)
[16] GB 55006-2021, General code for steel structures[S]. Beijing: China Architecture & Building Press, 2021. (In Chinese)
[17] GB/T 6398-2017, Metallic materials-Fatigue testing-Fatigue crack growth method[S]. Beijing: China Standard Press, 2017. (In Chinese)
[18] ASTM E647, Standard test method for measurement of fatigue crack growth rates[S]. West Conshohocken, PA: American Society for Testing and Materials International, 1995.
[19] Hassan, GM. Deformation measurement in the presence of discontinuities with digital image correlation: A review[J]. Optics and Lasers in Engineering, 2021(137): 106394.
[20] Sih GC, Barthelemy BM. Mixed mode fatigue crack growth predictions[J]. Engineering Fracture Mechanics, 1980,13(3): 439-451.
[21] Sih GC, Faria LDO. Fracture Mechanics Methodology[M]. Springer Netherlands, 1985.
[22] Choi DH, Choi HY . Fatigue life prediction of out-of-plane gusset welded joints using strain energy density factor approach. Theoretical and applied fracture mechanics, 2005, 44(1):16-26.
[23] Choi DH, Choi HY & Lee D. Fatigue life prediction of in-plane gusset welded joints using strain energy density factor approach. Theoretical and applied fracture mechanics, 2006, 45(2):108-116.
[24] Sih GC, Tang KK. Assurance of reliable time limits in fatigue depending on choice of failure simulation: energy density versus stress intensity[J]. Theoretical and applied fracture mechanics, 2011, 55(1):39-51.
[25] Liao X, Wang Y, Qian X, et al. Fatigue crack propagation for Q345qD bridge steel and its butt welds at low temperatures[J].Fatigue & Fracture of Engineering Materials & Structures, 2018, 41(3):675-687.
[26] Tan HM, Hu XQ, Huang D, et al. Fatigue crack propagation performance of Q690 high-strength steel and butt welds[J].Theoretical and Applied Fracture Mechanics, 2023, 126:103988.
[27] Shen X, Gao X, Shao Y, et al. Investigation on the fatigue crack growth behavior of welded joints in EH690 high-strength marine steel[J]. International Journal of Fatigue, 2024,189: 108572.
[28] Lukacs J, Dobosy A, Gaspar M. Fatigue crack propagation limit curves for S690QL and S960M high strength steels and their welded joints[J]. Advanced Materials Research, 2018, 1146(1):44–56.
[29] Wang H, Su B, Hua G, et al. Experiment research on corrosion fatigue crack propagation of marine engineering equipment material E690 high strength steel[J]. Hot Working Technol, 2016, 45(16). (In Chinese)
[30] Yang X, Fan W, Li Z, et al. Experimental and model study on corrosion fatigue crack propagation of Q420B steel in acid rain condition[J]. China Civil Engineering Journal, 2023, 56 (2):1–11. (In Chinese)
[31] Wang Q, Yan Z, Liu X, et al. Understanding of fatigue crack growth behavior in welded joint of a new generation Ni-Cr-Mo-V high strength steel[J]. Engineering Fracture Mechanics, 2018,194:224–39.
[32] Zhong Y, Shao Y, Gao X, et al. Fatigue crack growth of EH36 steel in air and corrosive marine environments[J]. Journal of Constructional Steel Research, 2023, 210:108104.
[33] Duan L, Wang CS & Wang SC. Fatigue Crack Growth Rate Tests of High Performance Steel HPS 485W[C]. 13th International Conference on Fracture, 2013.
[34] Wang CS, Duan L, Zheng L, et al. Fatigue crack growth rate tests of high performance steel HPS 485W for bridges[J]. Engineering Mechanics, 2013:30(6), 212-216.
[35] Zong L, Shi G, & Wang Y. Experimental investigation and numerical simulation on fatigue crack behavior of bridge steel WNQ570 base metal and butt weld[J]. Construction and Building Materials, 2015, 77, 419-429.
[36] Schijve J. Fatigue of Structures and Materials[M]. Heidelberg: Springer Science & Business Media, 2001.
[37] Hobbacher, A. F. Recommendations for fatigue design of welded joints and components[M]. Vol. 47. Cham: Springer International Publishing, 2016.
[38] BS7910, Guide to methods for assessing the acceptability of flaws in metallic structures[S]. London: British Standards Institution, 2005
[39] AS, Det Norske Veritas. Fatigue design of offshore steel structures[M]. Rev. 3 (2011).
[40] Lotsberg I ,Sigurdsson G ,Fjeldstad A , et al. Probabilistic methods for planning of inspection for fatigue cracks in offshore structures[J].Marine Structures, 2016, 46167-192.
[41] Berger C, Blauel JG, Pyttel B, et al. FKM Guideline Fracture Mechanics Proof of Strength for Engineering Components, 2nd revised ed., English version[M], Forschungskuratorium Maschinenbau (FKM), Frankfurt am Main, 2004
[42] Hojo K, Takahashi Y. Comparison of fatigue crack growth curves of Japan, the United States, and European Union Code and Standards[J]. Journal of Pressure Vessel Technology, 2012(134): 031004.
[43] WES 2805, Method of Assessment for Flaws in Fusion Welded Joints With Respect to Brittle Fracture and Fatigue Crack Growth[S], 2007, Tokyo: The Japan Welding Engineering Society.
[44] ASME Boiler and Pressure Vessel Code, XI Rules for Inservice Inspection of Nuclear Power Plant Components[M], 2007, ASME Boiler and Pressure Vessel Committee Subcommittee on Nuclear Power.
[45] JSME S NA1-2008, Codes for Nuclear Power Generation Facilities-Rules on Fitness-for-Service for Nuclear Power Plants[S], 2008, JSME.